Journal of Neuroscience Methods 435 (2026) 110863

Contents lists available at ScienceDirect

Journal of Neuroscience Methods

journal homepage: www.elsevier.com/locate/jneumeth

Optical and functional characterization of parasitic light in a DLP-based optogenetic system for single-neuron control

Clara Zaccaria [a,*], Asiye Malkoç [a,b], Yasaman Heydari [a,c], Beatrice Vignoli [a,d], Marco Canossa [b], Lorenzo Pavesi [a]

[a] Department of Physics, University of Trento, Povo (TN), Italy
[b] Department of Cellular Computational and Integrative Biology (CIBIO), University of Trento, Povo (TN), Italy
[c] Center for Mind/Brain Sciences (CIMeC), University of Trento, Rovereto (TN), Italy
[d] Neuroscience Institute, National Research Council of Italy, Padova, Italy

ARTICLE INFO

Keywords:
Digital light processing
Optogenetics
Patterned photostimulation
Light leakage
Calcium imaging
Synaptic potentiation
Single-neuron stimulation

ABSTRACT

Background: Digital light processor (DLP)–based patterned illumination enables targeted optogenetic stimulation with high speed and flexibility. While these systems are routinely characterized by optical contrast and spatial resolution, the functional impact of residual light leakage on biological samples remains frequently overlooked. Establishing thresholds and mitigation strategies for this unintended illumination is essential for ensuring the reliability and precision of targeted photostimulation assays.

New method: We quantitatively characterized parasitic illumination in a standard DLP-based microscopy setup and evaluated its functional impact on ChR2-expressing neuronal cultures, ranging from subthreshold depolarization to downstream effects on network-level plasticity. Leakage intensities were measured across multiple system configurations and correlated with neuronal responses using calcium imaging and immunostaining of activity-dependent synaptic markers.

Results: The intrinsic DLP black-level emission and back-reflections at the sample plane were identified as the dominant leakage sources, and mitigation strategies were suggested. Functional assays showed that leakages below 50 $\mu W/mm^2$ induce detectable calcium responses without triggering synaptic strengthening, whereas higher intensities can drive spiking, alter network dynamics, and promote synaptic potentiation.

Comparison with existing methods: Previous studies characterizing DLP-based optogenetic systems did not focus on the physiological effects induced by parasitic light with illumination intensities below the conventional ChR2 activation threshold.

Conclusion: These findings establish thresholds for unintended optogenetic stimulation and provide a simple framework for mitigating parasitic illumination in DLP-based patterned-light optogenetic systems, thereby improving the precision and reliability of targeted photostimulation.

1. Introduction

Optogenetics modulates neuronal activity using light, with specificity conferred by the genetic expression of targeted photosensitive proteins (opsins) (Yizhar et al., 2011). This precision can be further enhanced by delivering excitation light in tailored spatial patterns, enabling selective activation of specific subsets of opsin-expressing cells (Ronzitti et al., 2017; Anselmi et al., 2015). Various optical techniques and devices, including spatial light modulators (SLMs), digital micromirror devices (DMDs), LED arrays, and laser scanning approaches, are employed in both *in vivo* and *in vitro* experiments, enabling the creation of light patterns down to diffraction-limited resolution (S. Wang et al., 2007; Grossman et al., 2010; Zhu et al., 2012; Pandarinath et al., 2013; Sakai et al., 2013; Shim et al., 2016; Zhang et al., 2020; Bhatia et al., 2021; Bayat et al., 2022; Ronzitti et al., 2017; Anselmi et al., 2015). To ensure selective illumination on specific target areas, high contrast must be provided between the main excitation pattern and any secondary light reaching the sample. Typical issues tackled in the literature are artifacts like zero-order light leakages in holographic systems, out-of-focus excitation, and light scattering (Ronzitti et al., 2017, 2018). When dealing with 2D *in vitro* samples, spatial light modulation is often achieved with DMDs, as the simplest and cost-effective devices that can be easily coupled to microscopy setups (Ronzitti et al., 2017). Such systems, integrated into specific control boards with light sources

* Correspondence to: Department of Physics and Astronomy, University of Padova, Padova, Italy.
E-mail address: clara.zaccaria@unipd.it (C. Zaccaria).

https://doi.org/10.1016/j.jneumeth.2026.110863
Received 22 April 2026; Received in revised form 27 June 2026; Accepted 10 July 2026
Available online 23 July 2026

and optics – namely digital light processor devices (DLP) – can create patterns with a lateral spatial resolution down to 1 μm and a temporal resolution of less than 1 ms (Zaccaria et al., 2026; Pandarinath et al., 2013; Barral and Reyes, 2017; Anselmi et al., 2015). This precision is particularly valuable for selectively stimulating targeted neurons within complex neuronal networks, enabling the study of circuit functions (Auslender et al., 2025), and the emergence of coherent neuronal assemblies *in vitro* (Zaccaria et al., 2026).

In the literature, DLP-based illumination systems are commonly characterized in terms of intensity, spatial resolution, and contrast. However, a significant yet often underestimated challenge in these systems is light leakage, which can compromise spatial resolution through off-target illumination and induce unintended secondary effects on biological samples. Establishing thresholds and mitigation strategies for this unintended illumination is essential for ensuring the reliability and precision of targeted photostimulation assays. Previous studies have reported residual background illumination, which can induce measurable subthreshold responses in ChR2-expressing neurons (Barral and Reyes, 2017; Bhatia et al., 2021). This leakage primarily originates from the intrinsic DLP black-level emission, which creates a uniform, faint background underlying the primary spatial light pattern. Additional contributions from scattered and reflected light at the sample plane further complicate the control of the effective stimulus. Although typically low in intensity, these components may influence neuronal excitability and interfere with network-level assays. Despite the widespread adoption of DLP-based systems, the impact of such unintended illumination on *in vitro* neuronal networks remains poorly characterized.

In this work, we quantitatively characterize parasitic light sources in a DLP-based system integrated into an upright confocal microscope and evaluate practical mitigation strategies. Leveraging the experimental approach developed in Zaccaria et al. (2026), we examine the effects of low-intensity illumination on ChR2-expressing neuronal cultures using calcium imaging and immunostaining for activity-dependent markers. We hypothesize that light leakages at intensities below the conventional ChR2 activation threshold not only induce subthreshold modulation detectable by calcium imaging but may also influence network-level processes. In doing so, this study provides the technical characterization and validation needed to ensure the reliability of the biological experiments reported in Zaccaria et al. (2026), and establishes a methodological framework for characterizing parasitic illumination and validating illumination conditions for targeted optogenetic experiments.

2. Materials and methods

2.1. DLP and microscopy system

We optically aligned a DLP E4500 (Texas Instruments, model: DLP® E4500™ Evaluation Module) to an upright spinning-disk confocal microscope (Fig. 2(a)).

The microscopy setup consists of an Olympus BX63 upright microscope combined with a CrestOptics X-Light V2 Confocal spinning Disk Module with integrated VCS Super-resolution module, a Lumencore Spectra X LED based light engine, and a Prime BSI Back-illuminated 95% QE high-resolution Scientific CMOS camera (2048 × 2048 pixels).

The DLP system is equipped with 3 LEDs (red, green, blue), optics, a WXGA DMD (Wide Extended Graphics Array Digital Micromirror Device, 912 × 1140 mirrors), and a driver board including LED driver circuits and DLPC350 DMD controller. The DLP E4500 includes a QT-based GUI application for controlling the module via the USB interface. For this work, the blue LED with a wavelength of 460 ± 14 nm was used. The LED current, controlled by the system's graphic interface, was set to five levels delivering light powers of 0.39 ± 0.02 mW, 3.4 ± 0.2 mW, 8.0 ± 0.5 mW, 13 ± 1 mW, and 18 ± 1 mW on the sample plane. Power values were measured under the microsope objective, and errors represent standard deviations from repeated measurements across different experimental sessions; errors are omitted throughout the rest of the text for brevity.

Light exiting the DLP module is aligned to the EPI-fluorescence port of the microscopy setup through a 90 mm macro objective (SP 90 mm f/2.5, Tamron, Japan), after removal of the built-in collector lens. All the internal proprietary optics were removed, except for the final relay lens assembly, which acts like a projector tube lens element (Fig. 2(a)). Along this optical path, a field stop (FS) and an aperture stop (AS) diaphragm are present: the FS is used to reduce the field of view, while the AS is used to reduce aberrations. A dichroic mirror (Chroma T505lpxr-UF1) serves as a high-pass filter, reflecting wavelengths below 505 nm down to the microscope objective. 20× water immersion objective (UMPLFLN20XW, NA 0.5) and 10× dry objective (LMPLFLN10XLWD, NA 0.25) were used. The light distribution on the sample plane was optimized for maximum uniformity using 8-bit depth images. A single DLP mirror activation produces a 5.4 ± 0.2 μm diameter light spot (full-width-half-maximum) at the sample plane using a 10× objective, which reduces to 0.9 ± 0.07 μm if 60× magnification is used (Zaccaria et al., 2026).

The light power on the sample plane was measured beneath the objectives using a power meter (Ophir Nova, PD300) and normalized to the illuminated area to determine the light intensity reaching the biological sample.

Light projection is temporally controlled via external triggering using a Rigol DG2052 function generator.

2.2. Cell cultures

Cortices were isolated from C57BL/6J mouse embryos at embryonic day 17 (E17). Cortical tissues were collected and placed in ice-cold Hank's balanced salt solution (HBSS, Gibco, Cat.No. 14175053) with 10 mM HEPES (Gibco, Cat.No. 15630049). The tissues were then incubated with 0.25% trypsin-EDTA (Gibco, Cat.No. 25200072) at 37 °C for 20 min. To neutralize the trypsin, 1 ml Dulbecco's modified Eagle's medium (DMEM, Gibco, Cat.No. 11885084), containing 10% fetal bovine serum (FBS, Thermo Fisher, Cat.No. 10270106) and penicillin-streptomycin was added (1X, Gibco, Cat.No. 15140163). The cortical cells were dissociated using a P1000 pipette, collected by centrifugation (1900 RPM for 5 min), and resuspended in DMEM supplemented with 10% FBS and P/S.

When needed, cells were transfected with 1.5 μg of DNA construct using the Amaxa Nucleofector system, following the manufacturer's guidelines (Synactive (SA-tdTomato): Construct 1: CAG-rtTA-IRES-tdTomato, Construct 2: TreP-Arc3'-Nend-PSDTag-Venus-HA-Arc5'UTR (Gobbo et al., 2017)). After transfection, the cells were plated on glass coverslips pre-coated with poly-L-lysine (0.1 mg/ml, Merck Millipore, Cat.No. P1399). Three hours after plating, the medium was replaced with Neurobasal (Gibco, Cat.No. 21103049) supplemented with B-27 (1X, Gibco, Cat.No. 17504044), penicillin-streptomycin (1X), and Glutamax (1X, Gibco, Cat.No. 35050061). Half of the culture medium was refreshed every 3–4 days. Cells transfected with SA-tdTomato were treated with 1 μg/ml of doxycycline (Merck Millipore, Cat.No. D9891) for 24 h before light stimulation.

Cells were infected after 3 days in vitro (DIV 3) with the adeno-associated virus pAAV-hSyn-hChR2(H134R)-EYFP, a gift from Karl Deisseroth (Addgene plasmid #26973-AAV9; http://n2t.net/addgene:26973; RRID:Addgene-26973)

In some experiments, TTX (1 μM, Tocris, Cat.No. 1069) was applied 20 min before light stimulation.

All experiments were conducted in compliance with the Italian Animal Welfare legislation (D.L.26/2014) that was implemented by the European Committee Council Directive (2010/63EEC) The procedures were approved by local veterinary authorities and the Italian Ministry of Health (3FAF3.N.1JY). C57BL/6J mice were used to obtain pregnant dams for embryonic primary cultures. Mice were housed under a 12-h light/dark cycle with food and water ad libitum.

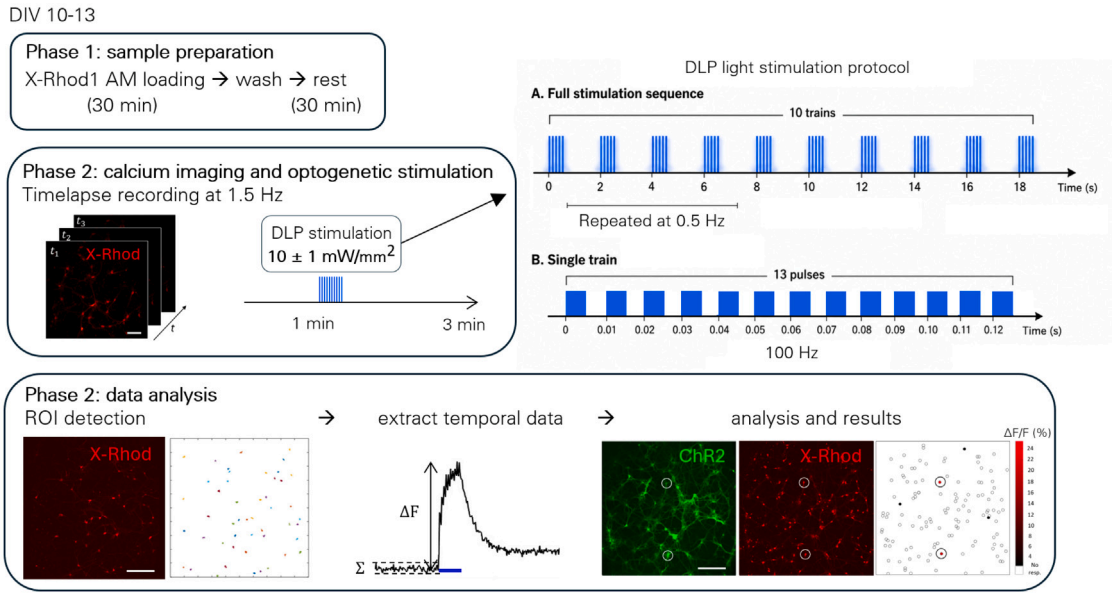

Fig. 1. Schematics of calcium experiment and optogenetic stimulation protocol. In the bottom panel, are represented colored ROI detected in the field of view, a representative calcium trace with analysis parameters and the illumination window (blue line), and ChR2 and X-Rhod images during a 2-spot illumination experiment. The heatmap illustrates the percentage change in fluorescence ($\Delta F/F$) calculated in the detected ROIs. Circles highlight the illuminated neurons. Scale bars: 100 μm.

2.3. Calcium imaging

At DIV 10–13, cells were treated with X-Rhod-1 AM (1 μM) in HBSS supplemented with $CaCl_2$ (2 mM) and $MgCl_2$ (1 mM) at 37 °C for 30 min. Subsequently, the cells were washed with supplemented HBSS at 37 °C. After 30 min, coverslips were positioned under the spinning-disk microscope in a 35 mm (transparent or black) dish with 2 ml of supplemented HBSS (recording medium). This volume ensures complete immersion of the coverslip while avoiding the formation of a meniscus at the liquid surface, which could induce imaging distortions. The green LED 550/15 nm from SPECTRA Light Engine was set to get 0.24 mW/mm^2 on the sample plane, to enable X-Rhod excitation, while avoiding spurious effects on the sample. The fluorescence intensity of X-Rhod was monitored by acquiring a timelapse at 1.5 Hz for about 3 min. At frame 100 of the timelapse, high frequency light stimulation (10 trains of 13 light pulses delivered at 100 Hz, repeated at 0.5 Hz, 50% duty cycle) from the DLP was applied. During the stimulation, the camera was triggered to acquire only when the DLP light was off (i.e., between the 10 light trains). Light excitation from the DLP was set at 10 ± 1 mW/mm^2, with field stop and aperture stop diaphragms properly positioned to improve image quality. In the case of spot excitation, compared to the characterization reported in Tables 1, the diameter of the back reflection ring slightly decreases to 550 ± 60 μm, while the intensity does not change significantly. Off-line analysis was performed with a MATLAB program for the regions of interest (ROI) detection and signal analysis (Zaccaria et al., 2026). Cell bodies were localized starting from X-Rhod basal fluorescent signal using Image Processing Toolbox with proper parameters control (area, centroid coordinates, axis dimensions, and intensity values), and pixels' value in each ROI was averaged in each frame to reconstruct the fluorescence temporal trace (Zaccaria et al., 2026). Each temporal calcium trace was normalized after a linear or exponential fit of the whole trace baseline, excluding the excitation window, selecting the best-fitting model based on the sum of squared errors. To classify traces as responses, we applied empirical threshold values to two parameters: the percentage increase of the fluorescence (F) above the baseline (F_0) during the stimulation window ($\Delta F/F = (F - F_0)/F_0$) and the ratio between this value and the maximum absolute variation of the fluorescence trace before the onset of the light stimulus (Σ). To classify a response, $\Delta F/F$ was set to be greater than 0.02 and $(\Delta F/F)/\Sigma$ to be greater than 1.2. The percentage number of responding neurons in the field of view was computed as the number of neurons that respond to light excitation over the total number of localized ROI in the field. The overall experimental procedure is summarized in Fig. 1.

2.4. Synaptic potentiation experiments

At DIV 11–13, cortical neurons were placed in a 35 mm dish with a dark bottom, filled with recording medium. Neurons were selected for individual excitations based on the expression of tdTomato (reporting SA) and YFP. Light excitations were administered using a pattern of 10 trains of 13 light pulses delivered at 100 Hz, repeated at 0.5 Hz with an intensity of 10 ± 1 mW/mm^2 (Zaccaria et al., 2026). After light stimulation, coverslips were returned to the incubator with culture media for 90 min, then fixed with cold 4% paraformaldehyde (PFA) for 20 min.

2.5. Immunocytochemistry

Fixed neurons were permeabilized with 0.1% Triton X-100 in PBS for 20 min and blocked with 3% bovine serum albumin (BSA) in PBS for 60 min. Neurons were incubated with primary antibodies diluted into 3% BSA at 4 °C overnight. After incubation, the cells were washed several times with 3% BSA and then incubated with fluorophore-conjugated secondary antibodies for 2 h at room temperature. The cells were then washed with PBS, counterstained with DAPI (Invitrogen), and mounted with Aqua Polymount (Polyscience Inc.). The primary antibodies were diluted as follows: RFP (Rockland #600-401-379) 1:1000, HA (Abcam #ab9111) 1:2000.

2.6. Confocal imaging and quantification of HA+ spines

Confocal imaging was performed using a laser-scanning motorized confocal system (Nikon A1) equipped with an Eclipse Ti-E inverted microscope and four laser lines (405, 488, 561 and 638 nm). Z-series images were taken with an inter-stack interval of 0.5 μm using a

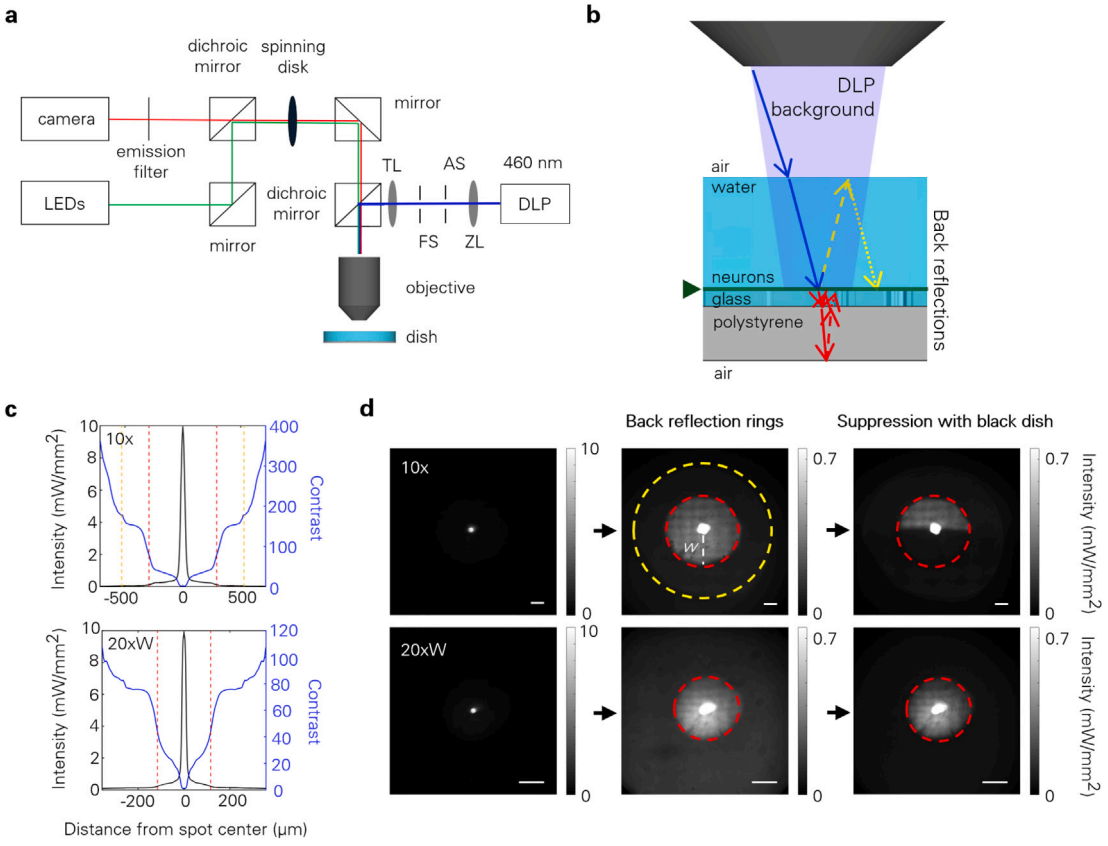

Fig. 2. (a) Sketch of the microscopy system (not in scale). Light exciting the DLP encounters a zoom lens (ZL) and a projector tube lens element (TL), passing by Aperture (AS) and Field (FS) Stops. (b) Schematic representation of DLP background and Back reflections occurring in the setup. Blue, red, and yellow arrows represent the light exiting the objective, its reflections at the interfaces below the sample plane, and the reflections at the liquid medium surface, respectively. The green triangle highlights the sample plane. Not in scale. (c) Representative intensity profiles for the 20 μm and 40 μm spots (10× and 20 × W objectives respectively): black curves show the azimuthally averaged intensity profile, while blue curves show the corresponding peak-to-local-intensity contrast profile. Red dashed lines indicate the measured extent of the first back-reflection ring, and for the 10× case, yellow dashed lines mark the extent of the second ring. (d) From left to right: image of a light spot projection on the sample plane with the 10× and 20 × W objectives; intensity histogram compression enables the visualization of back reflection rings induced by liquid medium (yellow circle) and the different layers beneath the sample plane (red circle, with ring annulus width w); suppression effect of back reflections using half-colored black dish. Scale bars: 100 μm.

60X oil immersion objective (Nikon APO 60x 1.4). Imaging processing was conducted using the NIS Elements software from Nikon. Confocal images underwent cropping, focusing on segments of dendrites proximal to the cell body within a 30–60 μm range. Subsequently, spines along the dendritic processes were morphologically identified using the tdTomato cellular filler. Manual quantification of spines expressing the HA signal (HA+) was performed on single-stack images, and the results were expressed as a percentage relative to the total number of spines for each cropped dendrite. Cells subjected to light stimulation were categorized as "targeted" neurons, while neighboring non-illuminated neurons within the field of view were designated as "FOV" cells. Cells located far from the stimulated area are classified as "Out-FOV". For each coverslip, the average HA+ spines percentage obtained in each cell was normalized over the average value obtained in OutFOV cells.

2.7. Quantification and statistical analysis

All statistical analyses were performed using GraphPad Prism version 10.0.0, GraphPad Software, Boston, Massachusetts USA, www.graphpad.com PRISM. All bar graphs and scatter plots depict average and standard deviation. Sample number n refers to the number of single experiments (fields of view, FOVs). On average, during calcium imaging, each experiment encompasses 127 ± 46 cells, whereas for each experiment on synaptic potentiation, on average, 13 ± 5 cells were analyzed. All presented data come from at least 3 preparations. Details on the type of statistical test used and the significance of the data are provided in the figure legends. A p-value smaller than 0.05 was considered statistically significant.

3. Results

The optical setup consists of a DLP E4500 projector, optically aligned to the EPI fluorescence port of an upright spinning-disk confocal microscope (Fig. 2(a)). Light leakages of the system and their effects on the sample plane were investigated and characterized using a 10× dry objective (10×) and a 20× water immersion objective (20×W). We classified two main leakage sources (Fig. 2): a fixed background exiting from the objective (*DLP background*), and the interaction of light with the setup components located beneath the sample plane (*Back reflections*):

- **DLP background.** This leakage component originates from the black level of the DLP, a faint light that exits the DLP module even when the mirrors of the DMD are positioned in off position. The intensity of such leakage on the sample plane depends on the DLP LED power as well as on the objective's specifications. It reaches maximum values of 9.6 ± 0.4 μW/mm^2 with the 10× objective and 30.5 ± 0.7 μW/mm^2 with the 20× objective. These values are comparable to the background light intensity previously reported by Barral et al. (2017) (Barral and Reyes, 2017).

- **Back reflections.** During the experiments, transparent glass coverslips hosting neuronal cultures are placed in a 35 mm transparent polystyrene plastic dish filled with recording medium. In such a system, light exiting the objective passes through multiple interfaces, including air (for dry objectives), liquid medium, glass, polystyrene, and air again. The boundaries between these different media can induce multiple reflections; being the system applied to 2D *in vitro* neuronal cultures, we consider the absorbance by the biological matter as negligible (Fig. 2(b,d)).

In the following, we will use the words *leakage* or *parasitic light* for any unintended illumination that reaches the sample in addition to the desired projected pattern. When referring to the specific leakage components, we will use *DLP background light* as the leakage coming from the DLP's black levels, and *back reflections* as the light reflected from the different interfaces on the sample plane.

3.1. Light leakage characterization during spot projections.

When a light spot is projected onto the center of the field of view (FOV), back reflections result in bigger rings concentric to the primary pattern. Fig. 2(d) illustrates the case for both dry and immersion objectives. In both cases, a more intense, inner ring originates from the reflections at the lower boundaries of the system (highlighted in red in Fig. 2(b,d)). With the dry objective, a second, larger ring is also formed by reflections at the surface of the liquid medium (highlighted in yellow in Fig. 2(b,d)). The dimension of these rings can be modeled using ray optics, ignoring for the sake of simplicity the effects of media absorption, the presence of the cell stratum, and multiple reflections. An estimate of the width (w) of the main ring annulus (the red ring in Fig. 2(d)) can be calculated as

$$w = 2\sum_i h_i tan\left(arcsin\left(\frac{NA}{n_i}\right)\right), \quad (1)$$

where h_i and n_i are the height and refractive index of the different layers, and NA is the objective numerical aperture (Fig. S1(a)).

Tables 1 and 2 summarize the measured dimensions and intensities of the back reflections for both objectives. A light spot with an intensity of approximately 10 mW/mm^2 was projected onto the center of the field of view. It had a full-width-half-maximum (FWHM) of about 20 μm with the 20×W objective and 40 μm with the 10× objective. Images were acquired with the microscope's CMOS camera and analyzed as described in Supplementary Materials. With the water immersion objective, a single ring is visible (Fig. 2(d)), which originates from the reflections at the glass-polystyrene. Solving Eq. (1) shows that a reflection at the polystyrene-air interface would create a ring annulus with w = 750 μm, which exceeds the field of view (FOV ≈ 666 × 666 μm^2) and is then not visible through the objective. The average intensity within the first ring annulus was 0.36 ± 0.08 mW/mm^2, while the intensity just outside the ring was 0.11 ± 0.04 mW/mm^2 (Table 2). Both values are higher than the DLP background measured in the same configuration (6.8 ± 0.7 $\mu W/mm^2$), confirming the additional role of back reflections in the system. With the dry 10× objective, the average intensity was measured to be 0.25 ± 0.06 mW/mm^2 in the first ring, 0.06 ± 0.01 mW/mm^2 in the second ring, and 33 ± 14 $\mu W/mm^2$ in the area immediately outside the rings. Also in this case, the intensity values exceed the measured DLP background (9.6 ± 0.4 $\mu W/mm^2$). The contrast ratios reported in Table 1 and represented in Fig. 2(c) provide a quantitative measure of spatial selectivity during spot illumination. We define as constrast the ratio between the peak intensity and the other intensity values measures across the field of view. For both objectives, the contrast ratio at the first ring (peak/ring) decreases with increasing spot size: from 37 ± 10 at FWHM ∼ 14 μm to 18 ± 6 at FWHM ∼ 27 μm for the 20×W objective, and from 49 ± 15 at FWHM ∼ 29 μm to 25 ± 8 at FWHM ∼ 54 μm for the 10× objective. This degradation is consistent with the quadratic dependence of back-reflection intensity on spot dimensions (Fig. S1(b)), since larger spots deliver proportionally more optical power into the reflection path. In all configurations, the contrast ratio outside the first ring (peak/ext) exceeds the corresponding peak/ring value, confirming that the first ring represents the main contribution of light leakage.

The intensity of back reflections changes linearly with the DLP LED power (Fig.S1(c)) and, when multiple spots are projected at an inter-distance smaller than the sum of their first ring radii, it sums up in the overlapping region (Fig.S1(d)).

3.2. Light leakage suppression

To reduce the back reflections induced by the polystyrene-air interface, where the refractive index mismatch is highest, the outer base of the dish was painted with black acrylic color (Black dishes configuration). As shown in Fig. 2(d) and in Table 2, in the case of the 10× objective, the use of black dishes reduces the light intensity both within and outside the two rings: the intensities in the first and second ring become comparable (48 ± 6 $\mu W/mm^2$ and 36 ± 11 $\mu W/mm^2$), and the DLP background estimate becomes 14 ± 8 $\mu W/mm^2$, consistent with the direct DLP background measurement under the objective.

In the case of the 20×W objective, the use of the dark base does not cancel out the back reflection ring (Fig. 2(d)), and the intensity outside the ring in reduced more than inside it, resulting in 253 ± 73 $\mu W/mm^2$ within the ring, and 32 ± 12 $\mu W/mm^2$ outside it (Table 2): this is consistent with the nature of the reflections, being the visible ring induced by the reflections at the glass-polystyrene interface, as mentioned before. This is also confirmed by the peak/ring and peak/ext contrast values reported in Table 2. For the 10× objective, the peak/ring contrast improves from 35 ± 12 (transparent dish, Table 1) to 207 ± 34, directly reflecting the strong suppression of the polystyrene-air back reflection. The peak/ext contrast increases comparably, from 145 ± 69 to 292 ± 111. For the 20×W objective, the ring contrast improvement is more limited, consistent with the dominant ring originating at the glass-polystyrene interface, which is unaffected by blackening the outer dish base, while the exterior region benefits more substantially.

Overall, these results show that black dishes are most effective for the 10× objective, where the polystyrene-air interface is the primary reflection source, while for the 20×W objective the improvement in spatial contrast is largely confined to the region beyond the ring.

3.3. Light leakage effects investigation by calcium imaging

To investigate the possible effects of light leakage during optogenetic experiments, calcium imaging was performed on 11–13 DIV primary cortical neuronal cultures infected with AAV-ChR2(H134R)-YFP (hereafter referred to as ChR2), using the calcium indicator X-Rhod-1 AM (hereafter referred to as X-Rhod) (Paredes et al., 2008).

Experiments were performed using different illumination configurations:

- Half-field illumination on black dishes at varying light intensities (i.e., DLP LED powers), to characterize the calcium response as a function of ChR2 expression, using both 2 ml and 1 ml of recording medium, to assess the effects of back reflections at different liquid volumes;
- DLP background alone, i.e., projection of a black image onto the sample, using both transparent and black dishes, to assess the role of the background, independently of the main excitation patterns;
- Spot illumination, using both transparent and black dishes, to investigate the effect of DLP light leakages during single cell targeting optogenetic experiments.

During these experiments, light was delivered through the 10× objective, following a high frequency temporal pattern consisting of 10 trains of 13 light pulses at 100 Hz, repeated at 0.5 Hz (Zaccaria et al., 2026) (Fig. 1).

Table 1
Study on the first ring dimensions in the case of different light spot dimensions, projected with the 20×W and 10× objective. Contrast ratios are the ratio between the measured peak intensity (10 ± 1 mW/mm^2) and the average intensity within the first ring (peak/ring), and outside the first ring (peak/ext).

Obj	FWHM	S_W	w	First ring diameter (μm)		Contrast ratio	
	(μm)	(μm)	(μm)	Expected	Measured	peak/ring	peak/ext
20x	14 ± 1	44 ± 8	113	270 ± 8	233 ± 26	37 ± 10	78 ± 21
	21 ± 1	47 ± 7		273 ± 7	232 ± 24	25 ± 8	73 ± 23
	27 ± 1	49 ± 6		275 ± 6	252 ± 23	18 ± 6	66 ± 23
10x	29 ± 1	89 ± 7	370	829 ± 7	566 ± 67	49 ± 15	132 ± 47
	41 ± 1	97 ± 4		837 ± 4	585 ± 65	35 ± 12	145 ± 69
	54 ± 1	106 ± 3		846 ± 3	569 ± 81	25 ± 8	129 ± 86

Table 2
Study of back reflections' intensity within the 1st and 2nd ring, and outside (Out), in the case of transparent and black dish when projecting a spot with a FWHM of about 20 μm and 40 μm with a 20×W and 10× objectives, respectively. Contrast ratios are the ratio between the measured peak intensity (10 ± 1 mW/mm^2) and the average intensity within the first ring (peak/ring), and outside the first ring (peak/ext).

Obj	Transparent dish (μW/mm^2)			Black dish (μW/mm^2)			Contrast ratio (Black)	
	1st	2nd	Out	1st	2nd	Out	peak/ring	peak/ext
20x	359 ± 76	–	114 ± 37	253 ± 73	–	32 ± 12	40 ± 12	219 ± 122
10x	254 ± 64	63 ± 14	33 ± 14	48 ± 6	36 ± 11	14 ± 8	207 ± 34	292 ± 111

3.3.1. Half-field illumination

Experiments were performed in black dishes containing 2 ml of recording medium. In this configuration, the effect of the final interface reflections is minimized, while back reflections from the liquid medium and DLP background are still present. Forty percent of the field from the left side was illuminated with varying light intensities by varying the light power from 0.39 to 18 mW (Materials and Methods). The resulting patterns on the sample plane were analyzed to characterize the intensity profiles across the FOV (Supplementary Materials). We focused the analysis on three regions: the illuminated region on the left (L, defined as the region where intensity $\geq 70\%$), the middle one (Mid, defined as the region where intensity $\leq 15\%$ until x-coordinate 1500), and the far-right one (R, defined as the region after x-coordinate 1500) (Fig. 3(a)). The corresponding intensity values are reported in Fig. 3(b). Calcium traces were analyzed in the three regions for different light intensities. Responses were characterized by the percentage of responding cells (N) and the response magnitude ($\Delta F/F$) (Materials and Methods), as well as by their distribution relative to the ChR2 expression level (Supplementary Materials, Fig. S2(a,b). As shown in Fig. 3(c), the percentage of cells responding to light in region L was significantly higher compared to the Mid and R regions, reaching a plateau of nearly 60% at approximately 4 mW/mm^2. Data at 0.39 mW indicate that very few calcium responses (from 0 to 1%) are detected at about 3 μW/mm^2 (R region). Responses' intensities in the three regions are quite similar due to the high variability given by ChR2 expression levels and cell status, making a statistical difference among the three regions hard to detect (Fig. S2(c)).

To assess the contribution of reflections arising from the recording medium interface, additional experiments were performed by reducing the medium volume from 2 ml to 1 ml at light powers of 8 and 18 mW. Decreasing the liquid volume, and thus the thickness of the liquid layer in the dish, shortens the effective reflection paths, and results in an approximately one-order-of-magnitude reduction in light intensity in the Mid region (Fig. 3(d), Fig. S1(e)). Consequently, the previously observed significant difference in the percentage of responding cells between Mid and R regions is no longer detected at 1 ml.

3.4. DLP background and single cells illumination

To evaluate the effects of light leakages under conditions of smaller and more spatially selective stimulation patterns, DLP background projection and spot illumination targeting single neurons were performed, using both transparent and black dishes. Specifically, calcium imaging experiments were performed in the following conditions:

- FOV illumination with DLP background only, applied to both infected and not infected cells;
- Single neuron spot illumination in the FOV;
- Simultaneous spot illumination of two neurons, to assess the potential cumulative effect of multiple back reflections on the network activity.

The DLP background was projected onto the sample plane with an intensity of 9.6 ± 0.4 μW/mm^2.

Such faint illumination occasionally induced calcium responses; however, no significant differences were detected between transparent and black dishes, in either the fraction of responding neurons (N%) or in the response amplitude ($\Delta F/F$) (Fig. 4, DLP bg). In contrast, the same protocol applied to non-infected cells (5 experiments) did not evoke any detectable response, confirming that the observed activity arises from opsin activation induced by the DLP background, with a negligible contribution from spontaneous calcium activity or imaging-related artifacts.

Soma-targeted single cell illumination was performed using the spot pattern characterized in Section 3.1, with 2 ml of recording medium. The light intensity at the sample plane was set to approximately 10 mW/mm^2. Based on the pattern characterization, light leakage outside the illuminated spot ranged from approximately 63 to 254 μW/mm^2 when using the transparent dish, and from approximately 36 to 48 μW/mm^2 when using the black dish (Table 2).

Cells with YFP fluorescence levels higher than 200 units were selected for stimulation, to maximize the probability of successful excitation. In the experiments involving the stimulation of two neurons, light spots were positioned at an average distance of 702 ± 93 μm, to avoid possible overlapping of the first back reflection rings (Figure S1(d)). Results are summarized in Fig. 4. In both experimental conditions, illuminated neurons exhibited stronger responses compared to non-illuminated ones.

The responses detected in non-illuminated neurons did not differ from those induced by the DLP background alone, and showed no preferential spatial location relative to back reflection rings (Fig. S3). No statistically significant differences were found between experiments conducted with transparent or black dishes. This suggests that

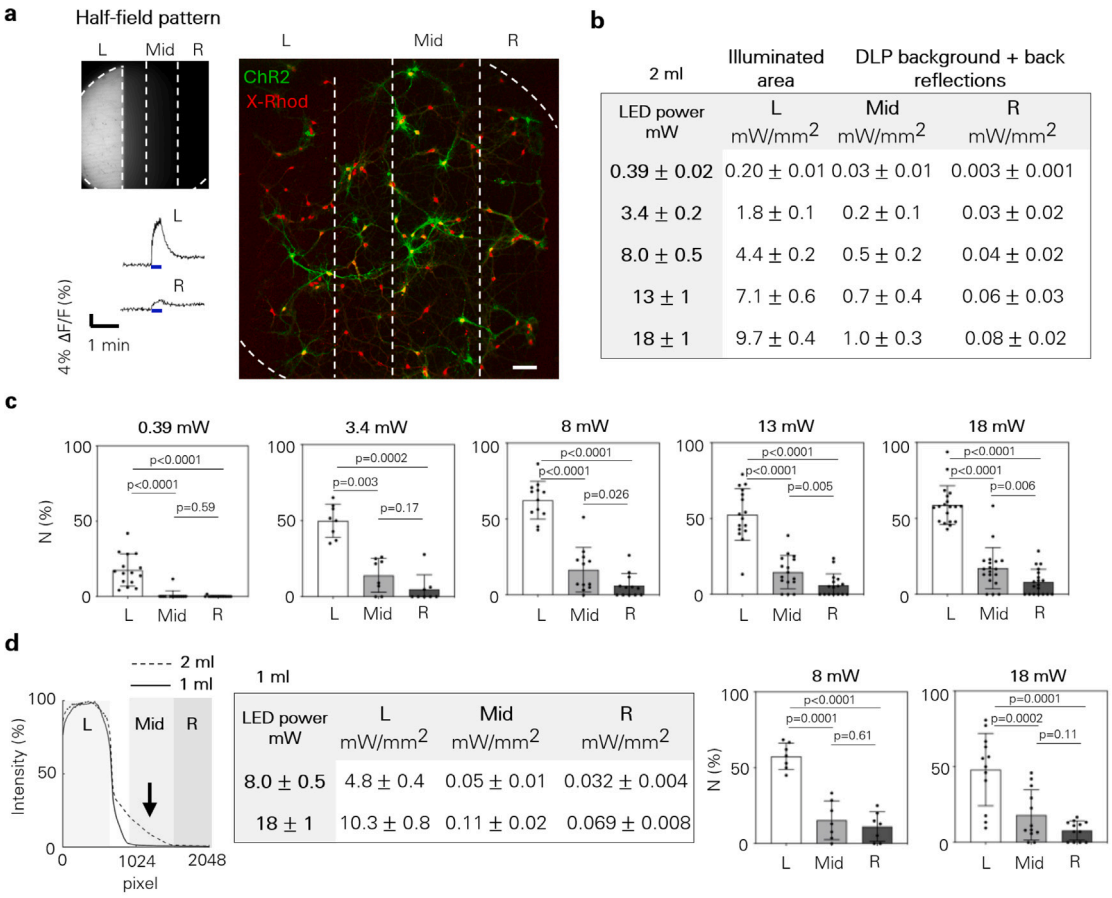

Fig. 3. (a) Half-field pattern projection on the sample plane, with highlighted L, Mid, and R regions. Below,Two representative calcium traces obtained in the L and R regions in the case of 18 mW light excitation (blue line). On the right, overlay images of ChR2 and X-Rhod signals are shown. Scale bar: 100 μm. (b) Light intensity values on the sample plane measured in the three regions for different DLP LED powers. (c) Calcium responses in the case of 2 ml of liquid volume in the dish. The percentage number of calcium responses obtained in L, Mid, and R regions is represented in bar graphs for different light powers (n = 15, 8, 12, 16, 19 FOVs for 0.39, 3.4, 8.0, 13, and 18 mW, respectively). Repeated Measurements one-way ANOVA Test. (d) Light distribution profile comparison in the case of 2 ml and 1 ml of liquid volume in the dish. The black arrow highlights the intensity change in the Mid region. The table shows the light intensity values on the sample plane measured in the three regions, for 8.0 and 18 mW with 1 ml. The percentage number of calcium responses obtained in L, Mid, and R regions is represented in bar graphs (n = 7, 12 FOVs for 8.0 and 18 mW). Repeated Measurements one-way ANOVA Test.

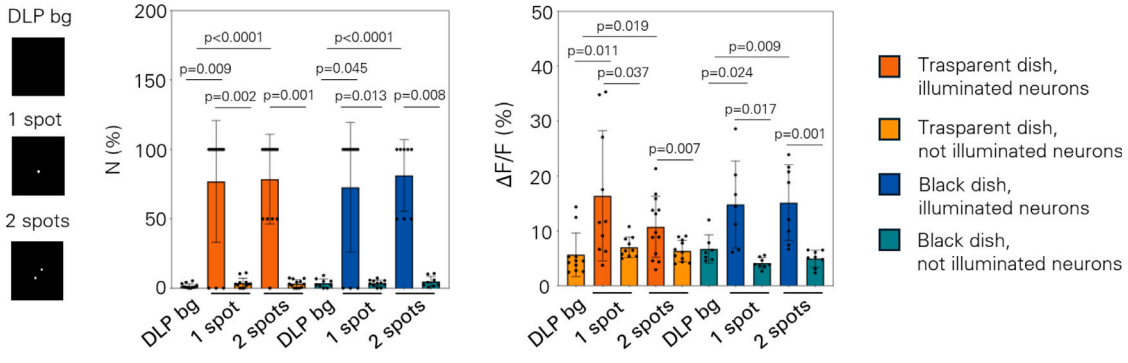

Fig. 4. On the left, examples of light patterns for DLP background (black image), 1 and 2 spot pattern projection are shown (not in scale). Bar graphs represent N and $\Delta F/F$ values obtained in the three different illumination cases, with transparent and black dishes. n = 13(9), 13(11), 14(11) FOVs for DLP background, 1 spot, and 2 spots respectively, with transparent(black) dishes. Statistical significance on N was determined using the Wilcoxon matched-pairs signed rank test on data coming from the same experiment, the Mann–Whitney test among non-stimulated and stimulated cells coming from different experiments, and the Unpaired t-test between not illuminated cells coming from different experiments. Statistical significance on $\Delta F/F$ was determined using a Paired t-test on data coming from the same experiments, and an Unpaired t-test on data coming from different experiments.

back-reflection rings in transparent dishes do not produce detectable effects in calcium imaging under our experimental conditions, although subtler subthreshold or network-level effects cannot be excluded.

3.5. Light leakages' effects on synaptic potentiation

Repeated, temporally correlated activation of neuronal pairs has been shown to promote synaptic strengthening under appropriate conditions (Zaccaria et al., 2026). Here, we investigate whether the leakage levels identified optically and by calcium imaging may be sufficient to affect this process. To this end, we quantify synaptic strengthening using an activity-dependent molecular marker (SA-tdTomato (Gobbo et al., 2017)) to determine whether parasitic light alone is sufficient to modulate plasticity in vitro. This approach was recently validated in Zaccaria et al. (2026) (Zaccaria et al., 2026), where the same DLP-based system was used to deliver high-frequency optogenetic stimulation to ChR2-expressing neuronal cultures, resulting in reliable synaptic potentiation between co-activated neurons. In that study, experiments were performed using black dishes, with a stimulation intensity of approximately 10 mW/mm^2 (leakage intensity ≤50 $\mu W/mm^2$, Table 2). Neuronal pairs within the field of view (FOV) were simultaneously illuminated using light spots with a full width at half maximum (FWHM) of approximately 40 μm using the same high frequency stimulation protocol used here. Results showed an increase in HA signal, reporting SA activation, exclusively on the spines of the two illuminated neurons, compared to non-illuminated neurons, both within the FOV, potentially exposed to light leakage, and outside the FOV (Out-FOV), where no DLP illumination is present. Notably, this effect was abolished by sodium channel blockade with Tetrodotoxin (TTX), indicating that neuronal communication is required for synaptic strengthening.

We investigated the specific contributions of light leakage in this context by analyzing whether unintended low-intensity illumination affects HA accumulation at dendritic spines. Experiments were performed using the same illumination protocol described in Zaccaria et al. (2026) (Zaccaria et al., 2026), comparing conditions employing black and transparent dishes. HA positive spines (HA+) were then quantified in illuminated (Targeted) and not illuminated neurons (FOV and Out-FOV). While the use of black dishes resulted in a reproducible selective increase in HA+ spines confined to targeted neurons, experiments performed with transparent dishes showed a significant increase in HA+ spines also in non-targeted neurons within the FOV (Fig. 5(b)). In both conditions, this effect was abolished by TTX, confirming its dependence on neuronal communication. Although these results might suggest that back reflections in transparent dishes directly induce widespread synaptic potentiation, further experiments were performed to isolate the contribution of light leakage alone. Specifically, we implemented a somatic-exclusion illumination protocol in which light spots were delivered within the FOV while avoiding direct somatic stimulation (Fig. 5(c)). Under these conditions, neurons were exposed to back reflected light, with intensities up to approximately 0.36 mW/mm^2 (Table 2), yet no significant increase in HA+ spines was observed in FOV neurons. Together, these findings indicate that parasitic light leakage alone, even if able to induce ChR2 activation, is not sufficient to induce synaptic strengthening within the network. However, it may facilitate network excitability and contribute to the formation of neuronal assemblies when multiple neurons are simultaneously targeted within the same FOV.

4. Discussion

DLP-based systems are widely used for optogenetic experiments on *in vitro* neuronal cultures and are commonly characterized by light intensity, spatial resolution, and contrast (Barral and Reyes, 2017; Pandarinath et al., 2013; Bhatia et al., 2021). However, light leakage is frequently overlooked during system characterization. Previous studies have reported residual background illumination in DLP-based setups in the range of tens of $\mu W/mm^2$. Barral et al. (2017) described a similar DLP system aligned to an upright microscope and measured a background intensity ranging from 10 and 50 $\mu W/mm^2$ (Barral and Reyes, 2017). Using patch-clamp recordings, they showed that this background light induced photocurrents insufficient to evoke action potentials but strong enough to elicit postsynaptic-like potentials of 0.1–1 mV (Barral and Reyes, 2017, 2016). Similarly, Bhatia et al. (2021) identified a residual light in a comparable setup (Bhatia et al., 2021). This faint light results mainly from the black level of DLP systems, a form of light leakage that occurs even when the projected image is black (i.e., micromirrors in off position). Consequently, when a spatial pattern is projected onto the sample, a continuous background illumination persists across the entire field of view, potentially confounding biological results. Furthermore, in thin neuronal cultures, light can diffuse through the medium and reflect at the underlying substrates, causing undesired illumination on the culture. These effects depend on experimental configuration and are difficult to quantify precisely.

Table 3
Summary of light leakage intensity regimes and their corresponding biological impact on ChR2-infected neuronal cultures.

Intensity regime	Main leakage source	Biological effect observed
< 3 $\mu W/mm^2$	DLP Background with optimized setup (low illumination intensity, black dish)	No significant calcium responses or synaptic changes observed.
10–50 $\mu W/mm^2$	DLP Background, minor back reflections (black dish)	Calcium transients detected; sufficient to modulate excitability but insufficient to induce expression of plasticity markers (HA+).
> 50 $\mu W/mm^2$	Back-reflections, transparent dish	Increased synaptic activity and significant risk of network-wide potentiation across the entire FOV.

In this work, we performed a systematic optical and functional characterization of parasitic light in a DLP-based optogenetic setup, identifying two primary leakage sources: intrinsic DLP background emission and back reflections at the sample plane. While intrinsic DLP background illumination was low (<30 $\mu W/mm^2$ at maximum with 20×W objective), back-reflections significantly amplified unintended illumination. In standard experimental conditions using transparent dishes, these light reverberation intensities can exceed 0.2 mW/mm^2. We investigated the effects of such light leakage on ChR2-infected *in vitro* neuronal cultures. ChR2 is indeed known to activate at intensities ranging between 0.1 and 1 mW/mm^2 (Grossman et al., 2010; Pandarinath et al., 2013; H. Wang et al., 2007; Aravanis et al., 2007), and possibly down to 0.01 mW/mm^2 when high expression levels are combined with high channel conductance (Grossman et al., 2011). However, higher intensities are generally associated with increased precision in single action potential induction (Berndt et al., 2011). Considering that ChR2 saturates at intensities above 40 mW/mm^2 (Grossman et al., 2011), optogenetic experiments are commonly performed at 5–10 mW/mm^2 (Aravanis et al., 2007; Zhang et al., 2006; Boyden et al., 2005; Ishizuka et al., 2006; Erofeev et al., 2019).

Experiments were performed using a 10×dry objective, which introduces additional back reflections compared to immersion objectives. Moreover, its larger field of view enables the investigation of a greater number of cells.

Based on our results, we can categorize leakage effects into distinct threshold regimes (Table 3).

Importantly, the observed impact of parasitic light depends heavily on the specific readout technique employed. While calcium imaging is highly sensitive to depolarization events, it lacks the specificity to distinguish between subthreshold or suprathreshold activity as effectively as downstream molecular markers. Immunostaining of

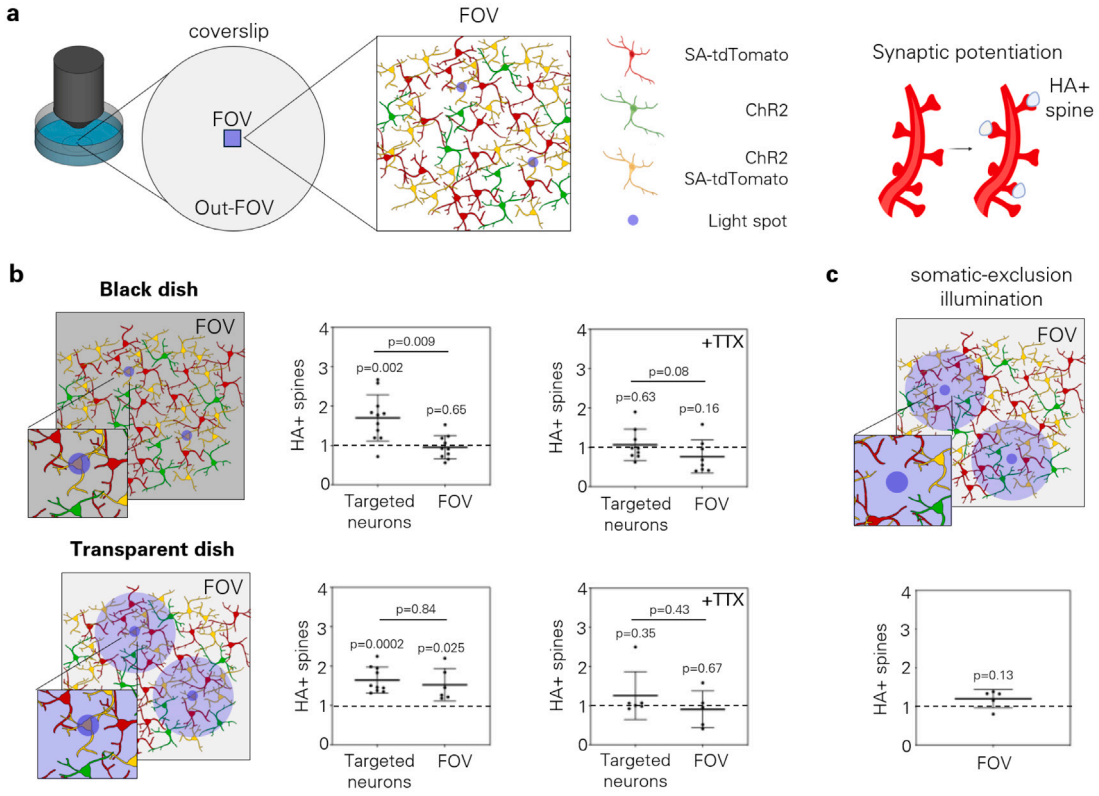

Fig. 5. (a) Schematic diagram of the experiments. In red are represented neurons successfully transfected with SA-tdTomato construct, in green the cells infected with ChR2, and in yellow cells expressing both constructs. (b) Schematic diagram of the illumination procedures for two-neuron illumination and respective results obtained with black dish (above) and transparent dish (below); n = 11(10) FOVs; +TTX: n = 9(6) FOVs for black (transparent) dish. (c) Somatic-exclusion illumination in transparent dishes; n = 5 FOVs. For each experiment, the percentage of HA+ spines was normalized over the average percentage measured in Out-FOV neurons. Each group underwent a One-sample t-test to the reference value 1 (dotted line). A Paired t-test was performed among groups. Analysis was performed on a combined dataset comprising a few samples from Zaccaria et al. (2026) and newly acquired data.

activity-dependent synaptic markers can reveal the potential impact of subthreshold activity. This becomes critical when investigating the 50 $\mu W/mm^2$ threshold. Literature reports that intensities as low as 0.02 mW/mm^2 may induce only subthreshold activation (H. Wang et al., 2007; Barral and Reyes, 2017). Accordingly, in our experiments, selective synaptic potentiation between simultaneously targeted neurons was preserved only when leakage was kept below 50 $\mu W/mm^2$ (black dish case, Fig. 5(b)). Although 0.2 mW/mm^2 leakage in transparent dishes did not induce network-wide potentiation alone, potentiation emerged when multiple neurons were targeted with high-intensity stimulation (Fig. 5(b)). This suggests that such leakage facilitates network excitability and amplifies signal propagation when combined with direct stimulation. While 0.2 mW/mm^2 induces spike generation (H. Wang et al., 2007), higher intensities are needed for precise single action potentials (Berndt et al., 2011), enabling potentiation. These findings reveal that, under our experimental conditions, low leakage can affect neuronal physiology, inducing subthreshold depolarization that biases excitability and confounds network-level readouts and plasticity interpretations.

The ChR2(H134R) variant used here exhibits reduced desensitization, slightly increased light sensitivity, and slower channel closing compared to wild-type ChR2, further emphasizing the relevance of low-intensity leakage and reducing the temporal precision of single-action-potential (Berndt et al., 2011; Lin, 2011; Lin et al., 2009). Newer variants present distinct trade-offs in low-light environments. High-photocurrent and ultra-sensitive variants (Chrimson, ChRmine, and ChRger) radically lower the threshold for low-intensity excitation; however, this sensitivity may increase their susceptibility to unintended activation from system light leakage or optical cross-talk (Klapoetke et al., 2014; Sridharan et al., 2022). Conversely, fast-kinetics variants (Chronos and ChRoME) are highly resilient against a continuous, low-intensity illumination, since they require much higher peak excitation intensities to achieve reliable activation (Klapoetke et al., 2014; Marshel et al., 2019). Moreover, optogenetic responses vary with culture density, expression levels, neuronal maturity, network state, and stimulation protocols (Grossman et al., 2011, 2013; H. Wang et al., 2007; Foutz et al., 2012; Zhu et al., 2012; Yizhar et al., 2011). Therefore, the leakage thresholds reported here are specific to ChR2(H134R)-expressing cultures used in our experimental conditions. Opsins with higher photocurrent, higher light sensitivity, or different kinetics may respond to lower parasitic illumination, making system- and opsin-specific calibration essential for patterned optogenetic experiments.

We demonstrated that simple mitigation strategies can drastically improve signal-to-noise ratios. Black-bottom dishes absorb back-reflections, reducing leakage to levels suitable for selective illumination, while minimizing recording medium volume shortens the optical path for scattering, offering another tunable parameter for noise reduction. Although we focused on DLP-based systems in *in vitro* cultures, these principles extend to other patterned photostimulation approaches (SLMs, DMDs, LEDs), where finite contrast and scattering limit spatial selectivity. In any optogenetic setup, whether using 2D or 3D samples, system-specific black-level emission and secondary scattering must be evaluated using sensitive excitability readouts combined with stable network-level markers.

5. Conclusions

We provide a reproducible framework for evaluating and mitigating parasitic illumination in DLP-based optogenetic setups, extending beyond optical power measurements to assess physiological impacts. We

show that parasitic light in patterned illumination systems may compromise single-cell specificity, confound plasticity experiments, and lead to unintended network activation if not characterized and controlled. Our system's characterization shows that leakages of 10–50 $\mu W/mm^2$ are detectable via calcium imaging but insufficient to induce synaptic potentiation alone, while intensities exceeding 50 $\mu W/mm^2$ can produce significant nonspecific network effects. Detection and interpretation depend on readout sensitivity: calcium imaging reveals subthreshold activity, while synaptic markers assess how light leakage can compromise network selectivity. Optogenetic responses vary with opsin properties (expression, distribution, conductivity, kinetics), illuminated area, and cellular characteristics (Grossman et al., 2011, 2013; H. Wang et al., 2007; Foutz et al., 2012; Zhu et al., 2012; Yizhar et al., 2011). Consequently, universal activation thresholds are difficult to establish, necessitating system-specific characterization for selective targeting and high-resolution experiments. These findings underscore the need for rigorous light-delivery characterization in patterned optogenetic systems to ensure experimental fidelity and accurate neuronal network dynamics interpretation.

CRediT authorship contribution statement

Clara Zaccaria: Writing – review & editing, Writing – original draft, Visualization, Validation, Software, Methodology, Investigation, Funding acquisition, Formal analysis, Data curation, Conceptualization. **Asiye Malkoç:** Writing – review & editing, Validation, Methodology, Investigation, Formal analysis, Data curation, Conceptualization. **Yasaman Heydari:** Writing – review & editing, Investigation. **Beatrice Vignoli:** Writing – review & editing, Writing – original draft, Visualization, Validation, Supervision, Project administration, Methodology, Investigation, Conceptualization. **Marco Canossa:** Writing – review & editing, Writing – original draft, Visualization, Supervision, Project administration, Methodology, Funding acquisition, Conceptualization. **Lorenzo Pavesi:** Writing – review & editing, Writing – original draft, Visualization, Supervision, Project administration, Funding acquisition, Conceptualization.

Declaration of generative AI and AI-assisted technologies in the manuscript preparation process

During the preparation of this work, the authors used Google Gemini and OpenAI ChatGPT to improve language and readability. After using these tools, the authors reviewed and edited the content as needed and take full responsibility for the content of the publication.

Declaration of competing interest

The authors declare that there are no financial interests, commercial affiliations, or other potential conflicts of interest that could have influenced the objectivity of this research or the writing of this paper.

Acknowledgments

This project has received funding from the European Research Council (ERC) under the European Union's Horizon 2020 research and innovation program, grant number 788793-BACKUP to L.P., Progetti di Ricerca di Rilevanza Nazionale (PRIN)-Bando 2017, grant number 2017HPTFFCPRIN to M.C., Fondazione CARITRO Cassa di Risparmio di Trento e Rovereto, grant number 2022.0230 to C.Z. We thank Antonino Cattaneo for providing -TreP-Arc3'-Nend-PSDTag-Venus-HA-Arc5'UTR and CAG-rtTA-IRES-TdTomato constructs. We thank the Model Organism Facility at the Department of CIBIO (University of Trento). We thank Pietro Scauso for the fruitful collaboration and insightful discussions.

Appendix A. Supplementary data

Supplementary material related to this article can be found online at https://doi.org/10.1016/j.jneumeth.2026.110863.

Data availability

Data will be made available on request.

References

Anselmi, F., Banerjee, A., Albeanu, D.F., 2015. Patterned photostimulation in the brain. New Tech. Syst. Neurosci. 235–270.

Aravanis, A.M., Wang, L.-P., Zhang, F., Meltzer, L.A., Mogri, M.Z., Schneider, M.B., Deisseroth, K., 2007. An optical neural interface: in vivo control of rodent motor cortex with integrated fiberoptic and optogenetic technology. J. Neural Eng. 4 (3), S143.

Auslender, I., Letti, G., Heydari, Y., Zaccaria, C., Pavesi, L., 2025. Decoding neuronal networks: A reservoir computing approach for predicting connectivity and functionality. Neural Netw. 184, 107058.

Barral, J., Reyes, A. D, 2016. Synaptic scaling rule preserves excitatory–inhibitory balance and salient neuronal network dynamics. Nature Neurosci. 19 (12), 1690–1696.

Barral, J., Reyes, A.D., 2017. Optogenetic stimulation and recording of primary cultured neurons with spatiotemporal control. Bio-Protocol 7 (12), e2335–e2335.

Bayat, F.K., Alp, M.İ., Bostan, S., Gülçür, H.Ö., Öztürk, G., Güveniş, A., 2022. An improved platform for cultured neuronal network electrophysiology: multichannel optogenetics integrated with meas. Eur. Biophys. J. 51 (6), 503–514.

Berndt, A., Schoenenberger, P., Mattis, J., Tye, K.M., Deisseroth, K., Hegemann, P., Oertner, T.G., 2011. High-efficiency channelrhodopsins for fast neuronal stimulation at low light levels. Proc. Natl. Acad. Sci. 108 (18), 7595–7600.

Bhatia, A., Moza, S., Bhalla, U.S., 2021. Patterned optogenetic stimulation using a dmd projector. Channelrhodopsin: Methods Protoc. 173–188.

Boyden, E.S., Zhang, F., Bamberg, E., Nagel, G., Deisseroth, K., 2005. Millisecond-timescale, genetically targeted optical control of neural activity. Nature Neurosci. 8 (9), 1263–1268.

Erofeev, A., Gerasimov, E., Lavrova, A., Bolshakova, A., Postnikov, E., Bezprozvanny, I., Vlasova, O.L., 2019. Light stimulation parameters determine neuron dynamic characteristics. Appl. Sci. 9 (18), 3673.

Foutz, T.J., Arlow, R.L., McIntyre, C.C., 2012. Theoretical principles underlying optical stimulation of a channelrhodopsin-2 positive pyramidal neuron. J. Neurophysiol. 107 (12), 3235–3245.

Gobbo, F., Marchetti, L., Jacob, A., Pinto, B., Binini, N., Bisogni, F. Pecoraro, Alia, C., Luin, S., Caleo, M., Fellin, T., et al., 2017. Activity-dependent expression of channelrhodopsin at neuronal synapses. Nat. Commun. 8 (1), 1629.

Grossman, N., Nikolic, K., Toumazou, C., Degenaar, P., 2011. Modeling study of the light stimulation of a neuron cell with channelrhodopsin-2 mutants. IEEE Trans. Biomed. Eng. 58 (6), 1742–1751.

Grossman, N., Poher, V., Grubb, M.S., Kennedy, G.T., Nikolic, K., McGovern, B., Palmini, R.B., Gong, Z., Drakakis, E.M., Neil, M.A., et al., 2010. Multi-site optical excitation using chr2 and micro-led array. J. Neural Eng. 7 (1), 016004.

Grossman, N., Simiaki, V., Martinet, C., Toumazou, C., Schultz, S.R., Nikolic, K., 2013. The spatial pattern of light determines the kinetics and modulates backpropagation of optogenetic action potentials. J. Comput. Neurosci. 34, 477–488.

Ishizuka, T., Kakuda, M., Araki, R., Yawo, H., 2006. Kinetic evaluation of photosensitivity in genetically engineered neurons expressing green algae light-gated channels. Neurosci. Res. 54 (2), 85–94.

Klapoetke, N.C., Murata, Y., Kim, S.S., et al., 2014. Independent optical excitation of distinct neural populations. Nature Methods 11 (3), 338–346. http://dx.doi.org/10.1038/nmeth.2836.

Lin, J.Y., 2011. A user's guide to channelrhodopsin variants: features, limitations and future developments. Exp. Physiol. 96 (1), 19–25.

Lin, J.Y., Lin, M.Z., Steinbach, P., Tsien, R.Y., 2009. Characterization of engineered channelrhodopsin variants with improved properties and kinetics. Biophys. J. 96 (5), 1803–1814.

Marshel, J.H., Kim, Y.S., Machado, T.A., et al., 2019. Cortical layer-specific critical dynamics triggering perception. Science 365 (6453), eaaw5202. http://dx.doi.org/10.1126/science.aaw5202.

Pandarinath, C., Carlson, E.T., Nirenberg, S., 2013. A system for optically controlling neural circuits with very high spatial and temporal resolution. In: 13th IEEE International Conference on BioInformatics and BioEngineering. IEEE, pp. 1–6.

Paredes, R.M., Etzler, J.C., Watts, L.T., Zheng, W., Lechleiter, J.D., calcium indicators, Chemical, 2008. Methods 46 (3), 143–151.

Ronzitti, E., Emiliani, V., Papagiakoumou, E., 2018. Methods for three-dimensional all-optical manipulation of neural circuits. Front. Cell. Neurosci. 12, 469.

Ronzitti, E., Ventalon, C., Canepari, M., Forget, B.C., Papagiakoumou, E., Emiliani, V., 2017. Recent advances in patterned photostimulation for optogenetics. J. Opt. 19 (11), 113001.

Sakai, S., Ueno, K., Ishizuka, T., Yawo, H., 2013. Parallel and patterned optogenetic manipulation of neurons in the brain slice using a dmd-based projector. Neurosci. Res. 75 (1), 59–64.

Shim, E., Chen, Y., Masmanidis, S., Li, M., 2016. Multisite silicon neural probes with integrated silicon nitride waveguides and gratings for optogenetic applications. Sci. Rep. 6 (1), 22693.

Sridharan, S., Gajowa, M.A., Ogando, M.B., et al., 2022. High-performance microbial opsins for spatially and temporally precise perturbations of large neuronal networks. Neuron 110 (7), 1139–1155.e6. http://dx.doi.org/10.1016/j.neuron.2022.01.008.

Wang, H., Peca, J., Matsuzaki, M., Matsuzaki, K., Noguchi, J., Qiu, L., Wang, D., Zhang, F., Boyden, E., Deisseroth, K., et al., 2007. High-speed mapping of synaptic connectivity using photostimulation in channelrhodopsin-2 transgenic mice. Proc. Natl. Acad. Sci. 104 (19), 8143–8148.

Wang, S., Szobota, S., Wang, Y., Volgraf, M., Liu, Z., Sun, C., Trauner, D., Isacoff, E.Y., Zhang, X., 2007. All optical interface for parallel, remote, and spatiotemporal control of neuronal activity. Nano Lett. 7 (12), 3859–3863.

Yizhar, O., Fenno, L.E., Davidson, T.J., Mogri, M., Deisseroth, K., 2011. Optogenetics in neural systems. Neuron 71 (1), 9–34.

Zaccaria, C., Malkoc, A., Auslender, I., Heydari, Y., Canossa, M., Vignoli, B., Pavesi, L., 2026. Investigation of synaptic connectivity in functional in vitro neuronal assemblies. Cell Rep. Methods 6 (101265).

Zhang, F., Wang, L.-P., Boyden, E.S., Deisseroth, K., 2006. Channelrhodopsin-2 and optical control of excitable cells. Nature Methods 3 (10), 785–792.

Zhang, X., Yeh, F.-C., Ju, H., Jiang, Y., Quan, G.F.W., VanDongen, A.M., 2020. Familiarity detection and memory consolidation in cortical assemblies. Eneuro 7 (3).

Zhu, P., Fajardo, O., Shum, J., Schärer, Y.-P. Zhang, Friedrich, R.W., 2012. High-resolution optical control of spatiotemporal neuronal activity patterns in zebrafish using a digital micromirror device. Nat. Protoc. 7 (7), 1410–1425.